Design of a Photonic Integrated Circuit for Swept-Source OCT for Simultaneous Operation in Two Distinct Wavelength Ranges

Ivan V. Stepanov*, Vladimir S. Lyubopytov, Anton A. Ivanov, and Elizaveta P. Grakhova
Ufa University of Science and Technology, 32 Zaki Validi str., Ufa 450076, Russian Federation
*e-mail: stepanov.iv@ugatu.su

Abstract. The paper presents a photonic integrated circuit (PIC) concept for the swept-source optical coherence tomography (SS-OCT) systems operating within two distinct wavelength ranges: 820–880 nm and 1260–1360 nm. The PIC features two interferometric schemes connected through a joint splitter that delivers a single output for tissue scanning. The proposed PIC concept is developed for the silicon nitride platform, which offers low losses compared to another photonic integrated platform. The numerical simulations were conducted using the Ansys Lumerical software to verify the PIC concept. The simulation results indicate that the focal length of the proposed SS-OCT system is approximately 2.9 mm for both wavelength ranges, and there is no interference between the optical signals from the adjacent interferometric systems.

Keywords: optical coherence tomography; photonic integrated circuits; swept-source OCT; dual-band OCT.

Paper #9190 received 20 Nov 2024; revised manuscript received 18 Dec 2024; accepted for publication 19 Dec 2024; published online 31 Jan 2025. doi: 10.18287/JBPE25.11.010301.

1 Introduction

Optical coherence tomography (OCT) prospects are highly positive, fueled by continuous technological advancements and expanding applications across various medical fields. OCT is a noninvasive method used to visualize the structure of biological tissues by analyzing the interference between an optical reference signal and the backscattered and backreflected signals from the sample being studied. Initially, OCT gained prominence in ophthalmology [1, 2], but its applications are now rapidly expanding. For instance, in cardiology, intravascular OCT images of coronary arteries provide high-resolution images of plaque morphology and stent deployment [3]. This technique aids in the diagnosis and treatment of coronary artery disease [4]. In dermatology, OCT is increasingly utilized for noninvasive skin imaging [5], assisting in the diagnosis of skin cancers [6], inflammatory skin diseases [7], and other dermatological conditions [8]. Additionally, emerging applications are being explored in gastroenterology (specifically, endoscopy), neurology, and other medical specialties.

Modern OCT systems offer significantly faster acquisition speeds and higher axial and transverse resolutions than earlier models. These advancements enable quicker examinations, minimize motion artifacts, and allow for the visualization of finer anatomical details. One notable example is swept-source OCT (SS-OCT), which provides much faster scan rates than spectral-domain OCT (SD-OCT) [9]. Despite these improvements, OCT still faces several challenges. The development of compact OCT systems, potentially utilizing photonic integrated circuits (PICs), is facilitating the creation of more accessible and portable devices well-suited for point-of-care applications and broader use in resource-limited settings [10]. Various solutions have already been proposed for the implementation of individual components within the PIC OCT system [11, 12] and for highly compact systems that are fully integrated [13]. Modern PICs incorporate SS-OCT [14–16] and SD-OCT [17, 18] methods and encompass all relevant wavelength ranges for medical applications, specifically 800 [12, 19], and 1310 nm [17, 20].

At the same time, another trend comprises searching for techniques to advance systems imaging speed, resolution (axial and transverse), and penetration depth. Such research focuses on using dual-band imaging schemes or integrating with other imaging modalities [21, 22], that can provide a more comprehensive picture of tissue structure and function.

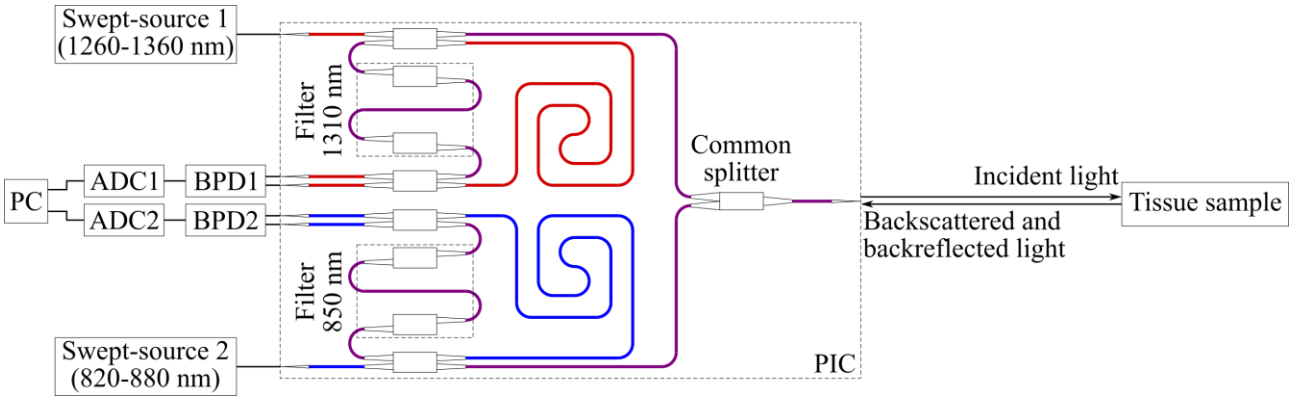

Fig. 1 Concept of a PIC-based dual-band SS-OCT system: PC – personal computer; ADC – analog-to-digital converter; BPD – balanced photodetector; PIC – photonic integrated circuit. Blue shows the waveguides in which radiation in the 820–880 nm wavelength range propagates, red – 1260–1360 nm, and violet – the waveguides in which both wavelength ranges can propagate.

The first approach seems particularly promising due to its simple integration with integrated photonics technology. Dual-band OCT presents significant benefits compared to single-band systems by utilizing different wavelengths that uniquely interact with tissue. This approach delivers complementary information, improving our tissue structure and function comprehension.

The applications of dual-band OCT are diverse and span various fields, with a significant focus on ophthalmology. In this field, dual-band OCT is particularly valuable for detailed retinal imaging, including angiography, blood flow measurement, and the assessment of retinal oxygen metabolism. It plays a crucial role in diagnosing and monitoring various eye diseases, such as glaucoma [23], where distinct differences can be observed in the OCT cross-sectional images at the two wavelengths used for the retinal nerve fiber layer. The dual-band OCT utilizes wavelengths of 840 nm and 1050 nm for visualizing the retina and the anterior segments of the eye [24].

Additionally, a second measurement in a different range enhances tissue contrast [25] and reduces image speckle, particularly in FD-OCT, while improving resolution [26]. For instance, visible light optical coherence tomography (Vis-OCT) offers superior axial resolution for imaging retinal layers, especially the retinal pigment epithelium and choroid complex. In contrast, near-infrared optical coherence tomography (NIR-OCT) provides greater penetration depth for examining deeper structures [27]. Moreover, the same research [27] has shown that Vis-OCT excels in measuring retinal blood oxygen saturation due to its increased blood optical absorption contrast in the visible spectrum.

In dermatology, researchers are exploring the use of dual-band line-field confocal optical coherence tomography (LC-OCT) systems that operate at wavelengths of 770 nm and 1250 nm. These systems aim to enhance the non-invasive diagnosis of malignant skin neoplasms, particularly basal cell carcinomas (BCCs). The dual-band approach integrates high-resolution imaging of superficial layers at 770 nm with deeper penetration capabilities at 1250 nm, resulting in a more comprehensive view of the lesion [28]. In cardiology, different wavelengths are employed to improve the differentiation of plaque components, such as lipid-rich areas versus fibrous tissue. However, it is essential to note that specific studies demonstrating this advantage need to be directly cited in the available data.

However, the lack of readily available publications detailing fully integrated dual-band OCT on PICs suggests that this is an area of ongoing research and development. While the building blocks for a PIC-based dual-band OCT system exist (dual-band OCT systems and PIC-based OCT systems), a fully integrated solution is not clearly documented in the provided data.

Thus, the paper presents the concept of a dual-band PIC designed for the most technologically relevant method – SS-OCT. We propose integrating two data collection schemes on a single chip, operating at two optimal wavelength ranges for medical applications: around 850 nm (820−880 nm) and around 1310 nm (1260−1360 nm). Both schemes capture backscattered and backreflected signals through a single output on the chip, ensuring data acquisition at varying depths and with different resolutions from a single observation point. The paper is organized as follows. Section 2 describes the concept of the system and the basic operating principle of the SS-OCT system on PIC. In Section 3, we present the design and simulation models for the system's building blocks. Section 4 describes the simulation results of the overall system performance, while Section 5 provides a discussion and main conclusions.

2 The Dual-Band OCT Scheme

Fig. 1 illustrates the concept of the proposed dual-band SS-OCT system. The chip is equipped with two tunable-source OCT circuits linked by a splitter, providing a single scanning output across both wavelength ranges.

The operating principle for both circuits, which use two different wavelengths, is consistent across the chip. Therefore, this chapter will focus on the functioning of just one circuit. Light from a tunable laser source is

coupled to the chip through an edge coupler. A directional multimode interference coupler (MMI) splits the light beam into a sample arm and a reference arm. The light beam in the sample arm is directed to the tissue sample via a joint splitter and decoupled from the PIC through the output edge coupler. The backscattered and backreflected light from the tissue sample is then collected by the chip using the same edge coupler. The signal is divided by a joint splitter into two interference circuits. Before reaching the MMI, the signal passes through a filter in each circuit. Ultimately, the backscattered and backreflected radiation interferes with the reference signal in the subsequent MMI. A balanced photodetector then converts the interference result into an electrical signal.

The PIC design is optimized for the silicon nitride platform, which exhibits lower losses than other integrated photonics platforms [29].

3 The PIC Components Design and Simulation

Numerical methods, specifically the finite difference eigenmode (FDE) and the eigenmode decomposition (EME) methods, were employed to simulate the components of the PIC for dual-band SS-OCT.

3.1. The Waveguide Cross-Section for Both Wavelength Ranges

The essential step in any PIC design is defining the waveguide cross-section, which facilitates light transmission between different components. The proposed device utilizes strip waveguides that are 450 nm in height. To determine the appropriate width of these waveguides, graphs were created to illustrate the relationship between the effective refractive index of the modes supported by the waveguide and its width. The resulting graphs for the central wavelengths of 850 nm and 1310 nm from the light sources are displayed in Figs. 2 and 3, respectively.

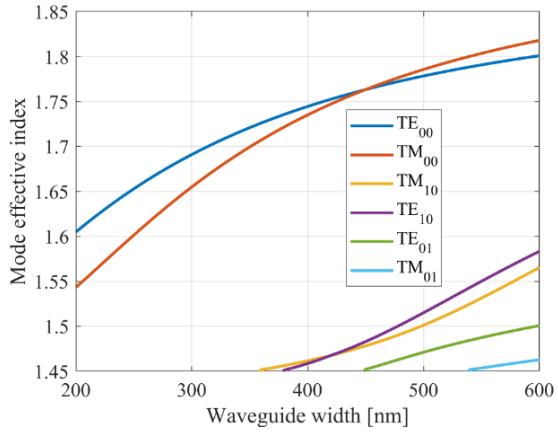

Fig. 2 The effective index of transverse modes in a waveguide versus its width for 850 nm central wavelength. TE indicates the transverse electric modes and TM − the transverse magnetic modes.

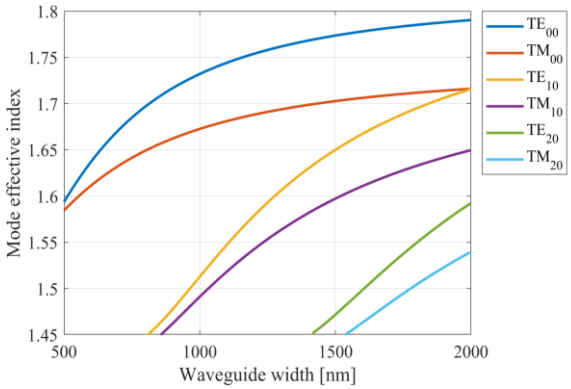

Fig. 3 The effective index of transverse modes in a waveguide versus its width for 1310 nm central wavelength. TE indicates the transverse electric modes and TM − the transverse magnetic modes.

The effective refractive index dependencies indicate that to achieve quasi-single-mode operation, the waveguide widths should be specified as follows: 500 nm for the wavelength range of 820–880 nm and 1200 nm for the wavelength range of 1260–1360 nm.

3.2 Design of the 50/50 MMI for Both Wavelength Ranges

The circuit splits the light beam using MMI, where the power distribution follows the self-imaging principle [30]. Fig. 4 illustrates the generalized structure of the MMI. The EME method was employed to determine the geometry of the MMI for 50/50 split ratios.

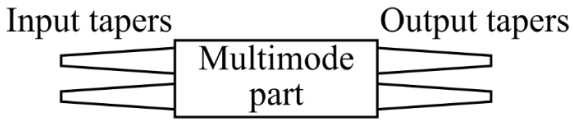

Fig. 4 Generalized structure of the MMI.

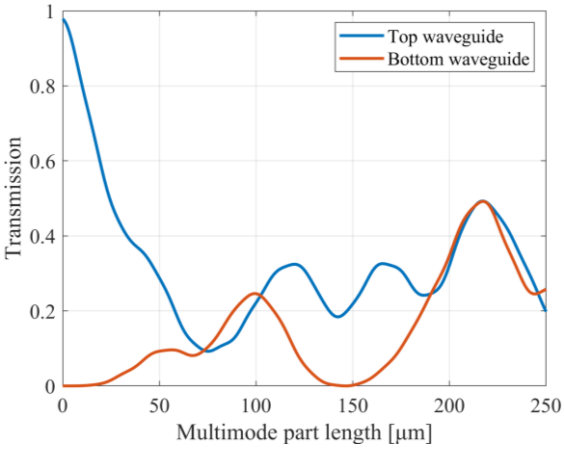

Fig. 5 The 50/50 MMI's transmission spectra relying on the length of the multimode section for a central wavelength of 850 nm.

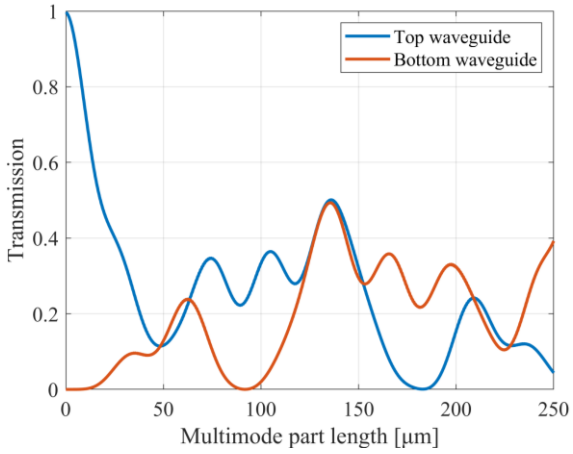

Fig. 6 The 50/50 MMI's transmission spectra relying on the length of the multimode section for a central wavelength of 1310 nm.

The width of the multimode section was set to 12 μm. The coordinates of the input waveguides were determined based on the principles outlined in Ref. [30]. Subsequently, the transmission coefficients from the upper left waveguide to the upper right and lower MMI waveguides were analyzed as a function of the length of the multimode section using the Ansys Lumerical MODE software package. The resulting data for central wavelengths of 850 nm and 1310 nm are presented in Figs. 5 and 6, respectively.

The optimal transmission point in both output waveguides determines the length of the multimode sections. At a central wavelength of 850 nm, the length was 217 μm, while at a central wavelength of 1310 nm, it was 141.2 μm. Fig. 7 illustrates the final geometry for both MMIs, while Figs. 8 and 9 show the transmission performance of the 50/50 MMIs across a broad wavelength range.

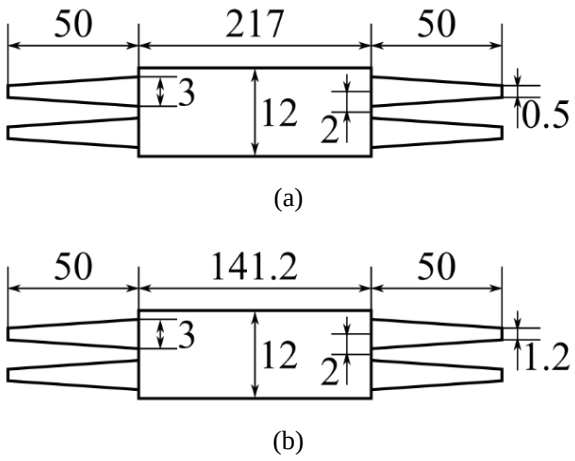

Fig. 7 50/50 MMI dimensions for (a) 850 nm and (b) 1310 nm central wavelengths. All dimensions are in μm.

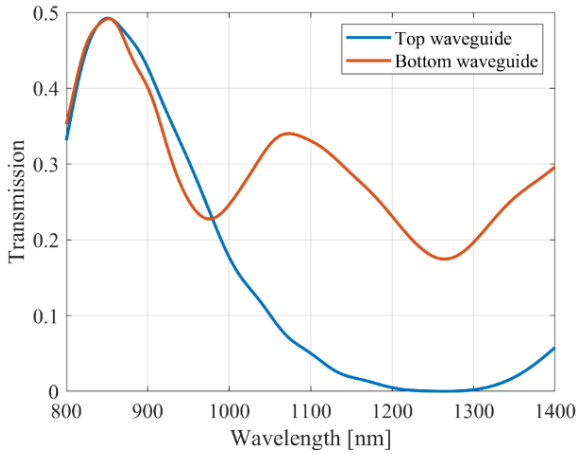

Fig. 8 Transmission spectra of the 50/50 MMI for an 850 nm central wavelength.

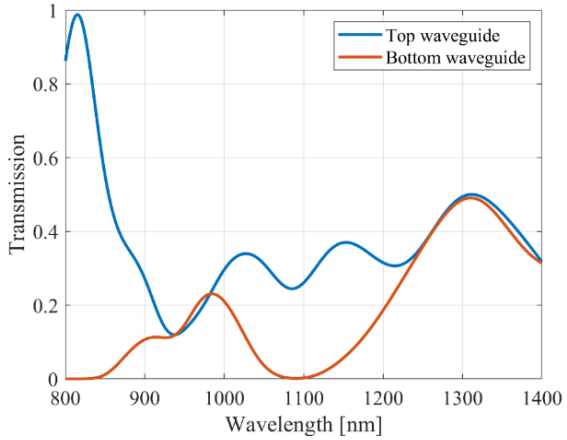

Fig. 9 Transmission spectra of the 50/50 MMI transmission spectra for a 1310 nm central wavelength.

3.3 The Splitter Design for Both Wavelength Ranges

An MMI-based joint splitter combines the interference schemes and divides the backscattered and backreflected radiation between them. The design follows the principles of a 50/50 MMI to determine its geometry. This splitter features a single input with a width set to 4 μm. As with the 50/50 MMI, we analyzed how the transmission coefficients depend on the length of the multimode section for both wavelength ranges (see Fig. 10). Consequently, the length of the multimode section was determined to be 15.1 μm by the maximum transmission for the both central wavelength. The dimensions of the joint splitter are illustrated in Fig. 11, while its transmission spectra are displayed in Fig. 12.

Joint splitter transmission spectra imbalance is conditioned by the different waveguides widths for the various wavelength ranges. Less waveguide width for the 820–880 nm wavelength range provides higher loss for the more abrupt waveguide taper. This effect does not have a significant impact on the system simulation.

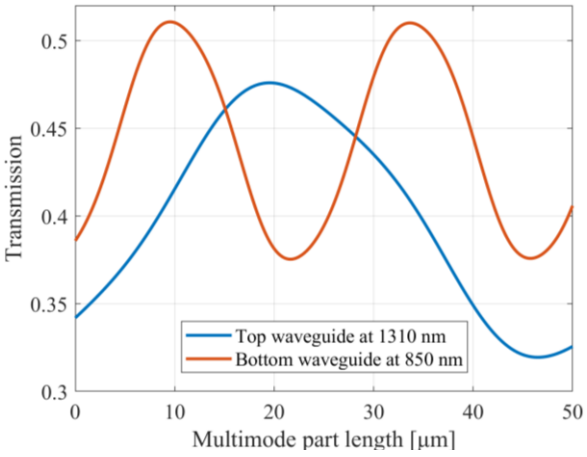

Fig. 10 Transmission spectra of the joint splitter over the length of the multimode section for central wavelengths of 850 nm and 1310 nm.

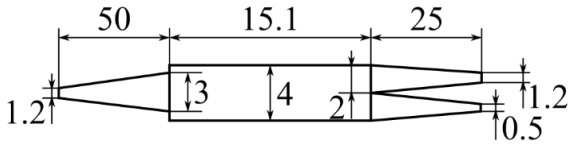

Fig. 11 The joint splitter dimensions in μm.

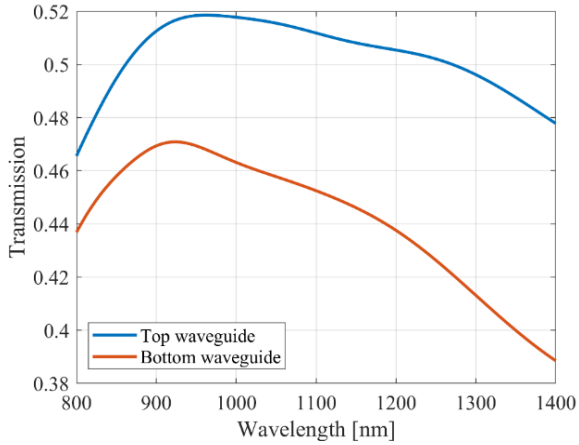

Fig. 12 Transmission spectra of a joint splitter over the broad wavelength band.

3.4 The Exponential-Shaped Edge Coupler

Light is coupled and decoupled from the PIC through an edge coupler, offering a wider bandwidth than traditional input-output gratings [31]. An exponential tapering shape was employed for the waveguide to enhance input efficiency. The length of the edge coupler is 200 μm, and a specific function can represent its shape:

$$y = \exp\left(\frac{\log(1.5)}{l}\cdot x\right) - 0.9 \text{ [um]},$$

where l is the length of the edge coupler, x denotes the coordinates along the X axis in the segment from 0 to l. The edge coupler width spans from 200 to 1200 nm.

Fig. 13 illustrates the transmission of the edge coupler. It is important to note that the transmission was measured for a mode spot with a diameter of 2 μm, positioned 5 μm from the PIC edge. For the edge coupler simulation, we used Ansys Lumerical EME software package.

Edge coupler simulation results show that average loss for the light coupling is approximately 3 dB. This value is sufficient for our simulation. But further light coupling optimization will provide higher OCT system sensitivity. Transmission spectra difference in this case is conditioned by the mode size inequality for the air and for the waveguide.

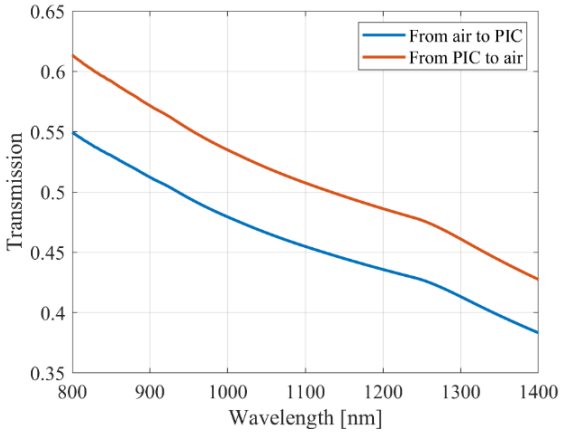

Fig. 13 Edge coupler transmission spectra.

3.5 Bandpass Filters

To effectively differentiate backscattered and backreflected radiation between two segments with distinct operating wavelength ranges, we propose utilizing a bandpass filter based on MMI within the device. These filters were developed utilizing the same principles as those used in the 50/50 MMI and the joint splitter. The key distinction in this case is that the device features only one input and one output. The geometries of the filters are illustrated in Fig. 14, while their transmission characteristics are shown in Fig. 15.

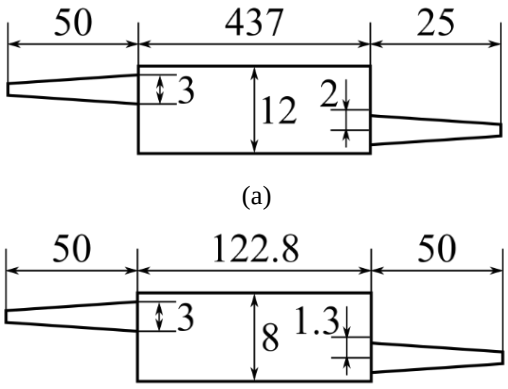

Fig. 14 Dimensions (in μm) of bandpass filters with central wavelengths of (a) 850 nm and (b) 1310 nm.

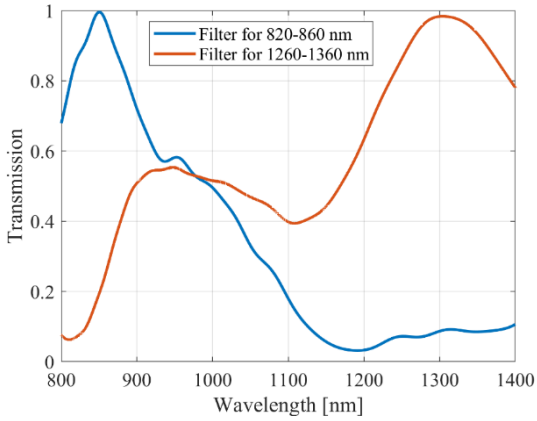

Fig. 15 MMI-based bandpass filters transmission spectra.

We chose bandpass filters lengths by the transmission spectra maximum for the needed wavelength range by analogy with the joint splitter geometry.

4 Simulation Results of the Performance of the PIC-Based Dual-Band SS-OCT System

To evaluate the performance of the SS-OCT system, we converted all the simulation results presented in the previous section of the article into S-parameters. We used the Ansys Lumerical INTERCONNECT software package to create a simulation model of the dual-band PIC. The following parameters were used in the model:

– Simulation time window: 10 ns;
– Sampling frequency: 250 THz;
– Radiation source tuning time: 10 ns;
– Output signal level at the radiation source: 0 dBm;
– Wavelength tuning ranges for the radiation sources: 820−880 nm and 1260−1360 nm;
– Signal attenuation level in waveguides: 92 dB/m [29].

A mirror with a reflectivity of 0.99 was used as a test sample to simulate biological tissue. It was connected to the circuit through a layer of air, the thickness of which was varied to determine the zero-delay point corresponding to the system's focal length.

The tuning time for the radiation sources was set to 10 ns to optimize resource usage. In commercial tunable radiation sources, this tuning time is typically 10 μs. However, we have previously demonstrated that while tuning time influences the frequency value, it does not affect the system's overall behavior [16, 32]. This assumption does not impact the signal level or the zero delay point.

The simulation results demonstrated the relationship between the OCT system's output signal frequency and the distance from the scanned sample to the end of the PIC. To establish this relationship, we identified the power peak in the signal spectrum and recorded the corresponding frequency in a data array. Fig. 16 illustrates this dependency.

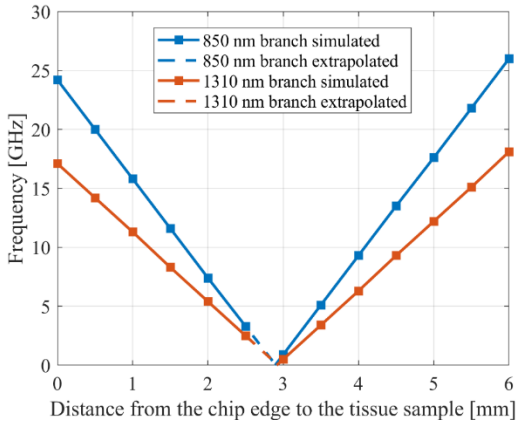

Fig. 16 The output signal frequency in relation to the distance between the scanned sample and the end of the PIC.

Based on the acquired data, extrapolation was conducted in a segment ranging from 2.5 to 3 mm to determine the precise value of the zero-delay point. As a result, the zero-delay point for the OCT branch with a central wavelength of 850 nm was found to be 2.9 mm. For the branch with a wavelength of 1310 nm, the zero-delay point value was 2.92 mm.

Figs. 17 and 18 illustrate examples of OCT signal spectra obtained from simulations at various distances between the scanned sample and the PIC edge.

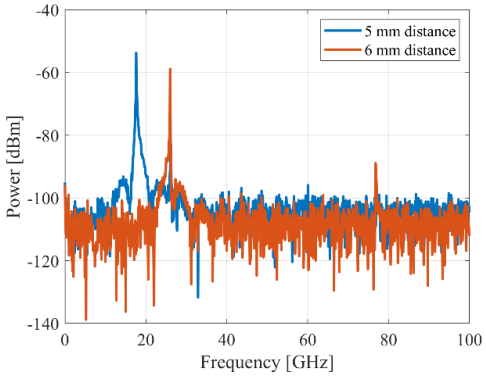

Fig. 17 OCT signal spectra for the branch with a central wavelength of 850 nm.

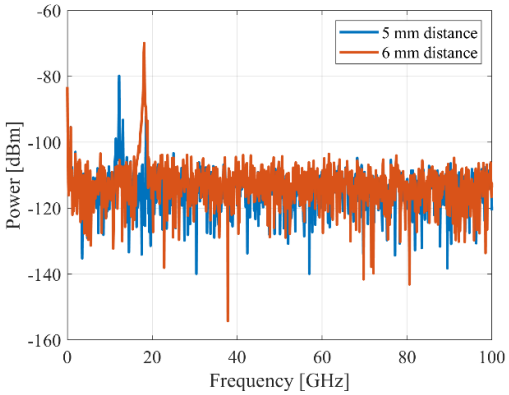

Fig. 18 OCT signal spectra for the branch with a central wavelength of 1310 nm.

The spectra show side frequency peaks. Supposedly, they arise due to the nonlinearity of the transfer characteristics of individual optical system components. It is worth noting that these peaks were also observed when using idealized bandpass optical filters that entirely suppress the adjacent frequency range in the shoulders of the sample.

5 Discussions and Conclusions

This paper presents a PIC concept for an SS-OCT system that can operate simultaneously in two different wavelength ranges: 850 nm and 1310 nm. Although initially designed for the silicon nitride platform, this PIC concept can also be adapted for other integrated photonics platforms. The chosen wavelength ranges are tailored to the most common OCT applications in medical diagnostics, including ophthalmology, dermatology, and endoscopic examinations. In each field, acquiring additional information about the biological tissue sample through measurements at a second wavelength can enhance resolution and increase visualization depth.

It is worth noting that biological tissues absorb radiation differently depending on the wavelength range [33]. This effect can be compensated with proper swept source power selection in the proposed scheme. However, medical standards must limit this power to prevent biological tissue damage.

The simulation results obtained using Ansys Lumerical software indicate that optical signals from adjacent interferometric systems do not interfere with one another. However, the distortions observed in the output signal spectrum for a single reflecting object are attributed to the nonlinear characteristics of individual components within the PIC.

To enhance the performance of dual-band SS-OCT PIC, it is crucial to improve the linearity of the transfer characteristics of its components within the specified operation bands. It can be achieved by optimizing the design of the elements based on MMI or by replacing them with broadband directional couplers [34]. However, using broadband directional couplers may increase the PIC's sensitivity to variations in characteristics due to manufacturing errors [35]. Furthermore, optimizing the edge couplers can help reduce attenuation during the coupling and decoupling of radiation to the PIC, thereby increasing the system's overall sensitivity.

The second step to improve the performance of the SS-OCT system is to enhance the functionality of the PIC. For both interferometric schemes, the focal length can be adjusted using a tunable reference arm, as previously demonstrated by the authors in an earlier study [32]. Furthermore, OCT systems with a tunable source can integrate a *k*-clock for analog-to-digital converters. This *k*-clock can be implemented either as an unbalanced Mach-Zehnder interferometer [32] or as a microring resonator [36], utilizing dispersion regions that exceed the wavelength range of the radiation source.

Another promising solution to improve OCT image quality is spectroscopic OCT (SOCT) signal processing algorithm realization at the personal computer side. This technique is based on the short-time and short-frequency Fourier transforms to create 2-D SOCT signals indexed by wavelength and depth in the object [37]. In combination with our PIC, it will allow obtaining more information about tissue samples [38].

Disclosures

The authors declare that they have no conflict of interest.

Acknowledgments

The research is supported by the Ministry of Science and Higher Education of the Russian Federation within the state assignment for UUST (agreement № 075-03-2024-123/1 dated 15.02.2024) and conducted in the research laboratory "Sensor systems based on integrated photonics devices" of the Eurasian Scientific and Educational Center.

References

1. J. Ong, A. Zarnegar, G. Corradetti, S. R. Singh, and J. Chhablani, "Advances in Optical Coherence Tomography Imaging Technology and Techniques for Choroidal and Retinal Disorders," Journal of Clinical Medicine 11(17), 5139 (2022).
2. R. Shen, L. K. Y. Chan, A. C. W. Yip, and P. P. Chan, "Applications of optical coherence tomography angiography in glaucoma: current status and future directions," Frontiers in Medicine 11, 1428850 (2024).
3. A. Murata, D. Wallace-Bradley, A. Tellez, C. Alviar, M. Aboodi, A. Sheehy, L. Coleman, L. Perkins, G. Nakazawa, G. Mintz, G. L. Kaluza, R. Virmani, and J. F. Granada, "Accuracy of Optical Coherence Tomography in the Evaluation of Neointimal Coverage After Stent Implantation," JACC: Cardiovascular Imaging 3(1), 76–84 (2010).
4. A. Karanasos, J. Ligthart, K. Witberg, G. Van Soest, N. Bruining, and E. Regar, "Optical Coherence Tomography: Potential Clinical Applications," Current Cardiovascular Imaging Reports 5(4), 206–220 (2012).
5. B. Wan, C. Ganier, X. Du-Harpur, N. Harun, F. M. Watt, R. Patalay, and M. D. Lynch, "Applications and future directions for optical coherence tomography in dermatology," British Journal of Dermatology 184(6), 1014–1022 (2021).
6. J. Olsen, L. Themstrup, N. De Carvalho, M. Mogensen, G. Pellacani, and G. B. E. Jemec, "Diagnostic accuracy of optical coherence tomography in actinic keratosis and basal cell carcinoma," Photodiagnosis and Photodynamic Therapy 16, 44–49 (2016).

7. G. Odorici, A. Losi, S. Ciardo, G. Pellacani, and A. Conti, "Non-invasive evaluation of Secukinumab efficacy in severe plaque psoriasis with confocal microscopy and optical coherence tomography: A case report," Skin Research and Technology 24(1), 160–162 (2018).
8. P. Gong, S. Es'haghian, K.-A. Harms, A. Murray, S. Rea, B. F. Kennedy, F. M. Wood, D. D. Sampson, and R. A. McLaughlin, "Optical coherence tomography for longitudinal monitoring of vasculature in scars treated with laser fractionation," Journal of Biophotonics 9(6), 626–636 (2016).
9. T. Kostanyan, G. Wollstein, and J. S. Schuman, "New developments in optical coherence tomography," Current Opinion in Ophthalmology 26(2), 110–115 (2015).
10. E. A. Rank, A. Agneter, T. Schmoll, R. A. Leitgeb, and W. Drexler, "Miniaturizing optical coherence tomography," Translational Biophotonics 4(1–2), e202100007 (2022).
11. L. Chang, N. Weiss, T. G. Van Leeuwen, M. Pollnau, R. M. De Ridder, K. Wörhoff, V. Subramaniam, and J. S. Kanger, "Chip based common-path optical coherence tomography system with an on-chip microlens and multi-reference suppression algorithm," Optics Express 24(12), 12635 (2016).
12. R. M. Ruis, A. Leinse, R. Dekker, R. G. Heideman, T. G. Van Leeuwen, and D. J. Faber, "Decreasing the Size of a Spectral Domain Optical Coherence Tomography System With Cascaded Arrayed Waveguide Gratings in a Photonic Integrated Circuit," IEEE Journal of Selected Topics in Quantum Electronics 25(1), 1–9 (2019).
13. J. Sancho-Durá, K. Zinoviev, J. Lloret-Soler, J. L. Rubio-Guviernau, E. Margallo-Balbás, and W. Drexler, "Handheld multi-modal imaging for point-of-care skin diagnosis based on akinetic integrated optics optical coherence tomography," Journal of Biophotonics 11(10), e201800193 (2018).
14. Y. Huang, M. Badar, A. Nitkowski, A. Weinroth, N. Tansu, and C. Zhou, "Wide-field high-speed space-division multiplexing optical coherence tomography using an integrated photonic device," Biomedical Optics Express 8(8), 3856 (2017).
15. E. A. Rank, S. Nevlacsil, P. Muellner, R. Hainberger, M. Salas, S. Gloor, M. Duelk, M. Sagmeister, J. Kraft, R. A. Leitgeb, and W. Drexler, "In vivo human retinal swept source optical coherence tomography and angiography at 830 nm with a CMOS compatible photonic integrated circuit," Scientific Reports 11(1), 21052 (2021).
16. I. V. Stepanov, E. A. Talynev, R. V. Kutluyarov, A. A. Ivanov, and E. P. Grakhova, "4-channel SS-OCT system design based on the silicon photonics chip with a high-scale integration," in Optical Technologies for Telecommunications 2022, A. V. Bourdine, O. G. Morozov, and A. H. Sultanov (Eds.), SPIE Proceedings 12743 (2023).
17. X. Ji, X. Yao, Y. Gan, A. Mohanty, M. A. Tadayon, C. P. Hendon, and M. Lipson, "On-chip tunable photonic delay line," APL Photonics 4(9), 090803 (2019).
18. E. A. Rank, R. Sentosa, D. J. Harper, M. Salas, A. Gaugutz, D. Seyringer, S. Nevlacsil, A. Maese-Novo, M. Eggeling, P. Muellner, R. Hainberger, M. Sagmeister, J. Kraft, R. A. Leitgeb, and W. Drexler, "Toward optical coherence tomography on a chip: in vivo three-dimensional human retinal imaging using photonic integrated circuit-based arrayed waveguide gratings," Light: Science & Applications 10(1), 6 (2021).
19. S. Nevlacsil, P. Muellner, A. Maese-Novo, M. Eggeling, F. Vogelbacher, M. Sagmeister, J. Kraft, E. Rank, W. Drexler, and R. Hainberger, "Multi-channel swept source optical coherence tomography concept based on photonic integrated circuits," Optics Express 28(22), 32468 (2020).
20. B. I. Akca, B. Považay, A. Alex, K. Wörhoff, R. M. De Ridder, W. Drexler, and M. Pollnau, "Miniature spectrometer and beam splitter for an optical coherence tomography on a silicon chip," Optics Express 21(14), 16648 (2013).
21. J. W. Evans, R. J. Zawadzki, R. Liu, J. W. Chan, S. M. Lane, and J. S. Werner, "Optical coherence tomography and Raman spectroscopy of the ex-vivo retina," Journal of Biophotonics 2(6–7), 398–406 (2009).
22. M. Tamošiūnas, O. Čiževskis, D. Viškere, M. Melderis, U. Rubins, and B. Cugmas, "Multimodal Approach of Optical Coherence Tomography and Raman Spectroscopy Can Improve Differentiating Benign and Malignant Skin Tumors in Animal Patients," Cancers 14(12), 2820 (2022).
23. X. Zhang, J. Hu, R. W. Knighton, X.-R. Huang, C. A. Puliafito, and S. Jiao, "Dual-band spectral-domain optical coherence tomography for in vivo imaging the spectral contrasts of the retinal nerve fiber layer," Optics Express 19(20), 19653 (2011).
24. S. Fan, L. Li, Q. Li, C. Dai, Q. Ren, S. Jiao, and C. Zhou, "Dual band dual focus optical coherence tomography for imaging the whole eye segment," Biomedical Optics Express 6(7), 2481 (2015).
25. F. Spöler, S. Kray, P. Grychtol, B. Hermes, J. Bornemann, M. Först, and H. Kurz, "Simultaneous dual-band ultra-high resolution optical coherence tomography," Optics Express 15(17), 10832 (2007).
26. M. Zhang, L. Ma, and P. Yu, "Dual-band Fourier domain optical coherence tomography with depth-related compensations," Biomedical Optics Express 5(1), 167 (2014).
27. S. Chen, X. Shu, J. Yi, A. Fawzi, and H. F. Zhang, "Dual-band optical coherence tomography using a single supercontinuum laser source," Journal of Biomedical Optics 21(6), 066013 (2016).
28. A. Davis, O. Levecq, H. Azimani, D. Siret, and A. Dubois, "Simultaneous dual-band line-field confocal optical coherence tomography: application to skin imaging," Biomedical Optics Express 10(2), 694 (2019).
29. R. S. El Shamy, M. A. Swillam, and X. Li, "Comparative Study of Photonic Platforms and Devices for On-Chip Sensing," Photonics 10(11), 1233 (2023).

30. L. B. Soldano, E. C. M. Pennings, "Optical multi-mode interference devices based on self-imaging: principles and applications," Journal of Lightwave Technology 13(4), 615–627 (1995).
31. F. Amanti, G. Andrini, F. Armani, F. Barbato, V. Bellani, V. Bonaiuto, S. Cammarata, M. Campostrini, T. H. Dao, F. De Matteis, V. Demontis, S. Donati, G. Di Giuseppe, S. Ditalia Tchernij, A. Fontana, J. Forneris, L. Frontini, R. Gunnella, S. Iadanza, A. E. Kaplan, C. Lacava, V. Liberali, L. Martini, F. Marzioni, L. Morescalchi, E. Pedreschi, P. Piergentili, D. Prete, V. Rigato, C. Roncolato, F. Rossella, M. Salvato, F. Sargeni, J. Shojaii, F. Spinella, A. Stabile, A. Toncelli, and V. Vitali, "Integrated Photonic Passive Building Blocks on Silicon-on-Insulator Platform," Photonics 11(6), 494 (2024).
32. I. V. Stepanov, E. A. Talynev, A. A. Ivanov, R. V. Kutluyarov, and E. P. Grakhova, "Design of a Photonic Integrated Device with an on-Chip k-Clock and Tunable Reference Arm for Swept-Source Optical Coherence Tomography," Journal of Biomedical Photonics & Engineering 9(3), 030317 (2023).
33. A. Sabeeh, V. Tuchin, "Recent Advances in the Laser Radiation Transport through the Head Tissues of Humans and Animals – A Review," Journal of Biomedical Photonics & Engineering 6(4), 040201 (2020).
34. G. F. R. Chen, J. R. Ong, T. Y. L. Ang, S. T. Lim, C. E. Png, and D. T. H. Tan, "Broadband Silicon-On-Insulator directional couplers using a combination of straight and curved waveguide sections," Scientific Reports 7(1), 7246 (2017).
35. Y. Fei, L. Zhang, T. Cao, Y. Cao, and S. Chen, "Ultracompact polarization splitter–rotator based on an asymmetric directional coupler," Applied Optics 51(34), 8257 (2012).
36. S. Kumar Bag, S. K. Varshney, "Ultrawide FSR microring racetrack resonator with an integrated Fabry–Perot cavity for refractive index sensing," Journal of the Optical Society of America B 38(5), 1669 (2021).
37. A. L. Oldenburg, C. Xu, and S. A. Boppart, "Spectroscopic Optical Coherence Tomography and Microscopy," IEEE Journal of Selected Topics in Quantum Electronics 13(6), 1629–1640 (2007).
38. M. Reddikumar, K. Bose, and R. Poddar, "Implementation of the swept source optical coherence tomography (SSOCT) system with a statistical method to analyze optical properties of turbid media," Optik 127(4), 1656–1659 (2016).